



Earing prediction with a stress invariant-based anisotropic yield function under non-associated flow rule

Saijun Zhang¹ · Yanshan Lou² · Jeong Whan Yoon³

Received: 26 August 2022 / Accepted: 1 March 2023 / Published online: 20 March 2023
© The Author(s), under exclusive licence to Springer-Verlag France SAS, part of Springer Nature 2023

Abstract

In this work, a recently proposed anisotropic Drucker function is implemented with non-associated flow rule (non-AFR) to predict the earing profile during cup drawing. The finite element formulation under non-AFR is developed for the precise simulation of the deep drawing process with a strong anisotropic aluminum alloy of AA2090-T3. The comparison between the simulation and experimental results reveals that the earing profile numerically predicted by the anisotropic Drucker function under non-AFR is in good agreement with the measured profile from experiments. It's also reveal that the improvement of accuracy of prediction for r-values does not always mean the synchronously improvement in prediction the earing profile for strong anisotropic phenomena of deep drawing for AA2090-T3. The computation efficiency of the anisotropic Drucker function is also investigated and compared with the Yld2004-18p function, which shows that 40% reduction of computational cost can be reached. The influence of different shapes of yield and potential on earing prediction is also investigated by combining the anisotropic Drucker function and Yld2004-18p function under non-AFR, which demonstrates that a proper shape of plastic potential is very important to predict the small ear around 0° for AA2090-T3. It also proves that both the yield and plastic potential functions strongly influence the height and earing profile in the simulation of cup deep drawing. It's also should be mentioned that the r-value does not keep constant in the simulation in the uniaxial tension of a single cubic element, but varies with the increase of plastic deformation in directional uniaxial tension, which may raise the difficulty for accurately prediction in metal forming.

Keywords Stress invariant · Anisotropy · Non-Associate flow rule · Earing · Cup deep drawing · Sheet metal forming

Introduction

Anisotropic plastic behavior is closely related with the deformation and formability of sheet metal. A proper yield function is very important to describe and predict the anisotropic plastic deformation with satisfactory accuracy. Various anisotropic yield functions have been proposed to model the anisotropy for sheet metals. After the first anisotropic yield function proposed by Hill [18], many non-quadratic anisotropic yield functions in forms of principal stresses [1, 2, 4–10, 13, 19, 21, 28, 31, 32], homogeneous polynomials [20, 41, 43] or stress invariants [11, 12, 30, 33, 40, 54, 55] were developed. Due to the simplicity of derivatives and easy implementation, the stress invariants based yield functions are very competitive with respect to computational costs compared to those based on the principal stresses in simulation of metal forming [30]. These phenomenological functions are generally used to predict the directional yield stresses and R-values simultaneously with the

✉ Saijun Zhang
mesjzhang@scut.edu.cn

Yanshan Lou
ys.lou@xjtu.edu.cn

Jeong Whan Yoon
j.yoon@kaist.ac.kr; j.yoon@deakin.edu.au

¹ Guangdong Provincial Key Laboratory of Precision Equipment and Manufacturing Technology, School of Mechanical and Automotive Engineering, South China University of Technology, Guangzhou 510640, China

² School of Mechanical Engineering, Xi'an Jiao Tong University, 28 Xianning Road, Xi'an 710049, Shaanxi, China

³ Department of Mechanical Engineering, Korea Advanced Institute of Science and Technology (KAIST), 291 Daehak-Ro, Yuseong-Gu, Daejeon 305-701, Republic of Korea

same function under associate flow rule (AFR). However, it is difficult to accurately describe the directionality of both yield stresses and R-values of materials with strong anisotropy due to limited number of parameters. In these cases, very complicated yield functions with more parameters such as Yld2004-18p [8] and CPB06-ex2 [13] are required to describe all the measured anisotropic quantities under AFR.

Another approach that can effectively model anisotropic plastic behavior is to use non-associated flow rule (non-AFR), which eliminates the restriction that plastic yielding and flow directions are controlled with same function. In non-AFR, two different functions or two separate sets of anisotropic coefficients with the same function are adopted to represent yielding and plastic potential respectively. Therefore, simple and efficient constitutive models under non-AFR can be used to describe the anisotropy with the same order of accuracy as obtained from the complicated models with AFR. For instance, the Hill48 [18] quadratic function under non-AFR were successfully utilized by different researchers, such as Stoughton [44], Cvitanic et al. [16], Stoughton and Yoon [46], Mohr et al. [35] and Taherizadeh et al. [47], to describe the anisotropic response for different materials. Another popular non-AFR model is based on Yld2000 function [7], which can correctly describe the highly anisotropic plastic behavior [17, 34, 36, 37, 51]. Besides, the strength differential effect can also be accurately modeled by the pressure sensitive non-AFR model proposed by Stoughton and Yoon [45] and Yoon et al. [54]. Detailed review of anisotropic yield function development can be found in Banabic et al.[3].

In the last decade, anisotropic hardening functions attracted a lot of attentions. Many analytically anisotropic hardening functions were proposed, such as Stoughton and Yoon [46], the coupled quadratic-non-quadratic functions by Park et al., [37], Lee et al. [29], Hu et al. [26], Hu and Yoon [25], Hu et al. [27], Hou et al. [22–24], Chen et al. [14] and Lou et al. [34]. These anisotropic hardening functions dramatically improve the modeling accuracy of anisotropic hardening behaviors with respect to plastic strain.

Earing is very common in cup drawing process of sheet metal and is widely used to evaluate and verify anisotropic plasticity models. Most of the anisotropic models mentioned above have been implemented into the finite element codes under AFR to predict the earing during cup drawing process [49–51]. Yoon et al. [52], Soare and Barlat [42] and Vrh et al. [48] applied advanced yield functions, such as Yld2004-18p [8], BBC2008 [15], homogeneous polynomials [43], to predict six or eight ears in the circular cup drawing of strong anisotropic materials. Earing prediction was also performed based on non-AFR including Yoon et al. [53], Park and Chung [36] and Safaei et al. [38] who successfully

got more than four ears in their numerical simulations for AA2090-T3 and AA5042.

In this paper, the newly proposed anisotropic Drucker function [30] is briefly reviewed and calibrated to model the directional yield stresses and R-values for AA2090-T3 under non-AFR. Then this function is implemented into ABAQUS/Explicit with semi-implicit integration algorithm under non-AFR, which is verified for uniaxial tension simulations of a single element in different orientations. The simulation of cup drawing of AA2090-T3 is performed and compared with the experiments to evaluate the performance of the anisotropic Drucker function. The computation cost relative to the Yld2004-18p is also investigated. In addition, the influences of the shapes of yield and potential surface on earing prediction is further investigated and discussed by combining the anisotropic Drucker function and Yld2004-18p function under non-AFR.

Anisotropic Drucker function

The following function was proposed by Lou and Yoon [30] by summing up n-components of the anisotropic Drucker function in a form of

$$f(\sigma_{ij}) = \tilde{\sigma} = \frac{1}{n} \sum_{m=1}^n \left\{ \left[\left(J_2^{(m)} \right)^3 - c \left(J_3^{(m)} \right)^2 \right]^{1/6} \right\} \quad (1)$$

Linear transformations are applied to each component of the function to capture the material anisotropy. It should be noticed that HCP materials that exhibit the strong strength-differential effect cannot be accurately described by this symmetrical yield function. In that case, the asymmetrical yield functions [12, 54] are suggested to be used for the proper modeling of the strength differential effect of HCP metals.

In Eq. (1), both the second invariant $J_2^{(m)}$ and the third invariant $J_3^{(m)}$ are functions of the linear transformed stress tensor $\mathbf{s}'^{(m)}$

$$J_2^{(m)} = \frac{1}{2} \mathbf{s}'^{(m)} : \mathbf{s}'^{(m)} = -s'_{11} s'_{22} - s'_{22} s'_{33} - s'_{11} s'_{33} + \left(s'_{12} \right)^2 + \left(s'_{23} \right)^2 + \left(s'_{13} \right)^2 \quad (2)$$

$$J_3^{(m)} = \det(\mathbf{s}'^{(m)}) = s'_{11} s'_{22} s'_{33} + 2s'_{12} s'_{23} s'_{13} - s'_{11} \left(s'_{23} \right)^2 - s'_{22} \left(s'_{13} \right)^2 - s'_{33} \left(s'_{12} \right)^2 \quad (3)$$

where the linear transformed stress tensor is defined as

$$\mathbf{s}'^{(m)} = \mathbf{L}^{(m)} \boldsymbol{\sigma} \quad (4)$$

with the linear transformation tensor $\mathbf{L}^{(m)}$ given as

Table 1 Normalized initial yield stresses and R-values of AA 2090-T3

yield stress	σ_0/σ_0	σ_{15}/σ_0	σ_{30}/σ_0	σ_{45}/σ_0	σ_{60}/σ_0	σ_{75}/σ_0	σ_{90}/σ_0	σ_b/σ_0
	1.0000	0.9605	0.9102	0.8114	0.8096	0.8815	0.9102	1.0350
r-values	r_0	r_{15}	r_{30}	r_{45}	r_{60}	r_{75}	r_{90}	r_b
	0.2115	0.3269	0.6923	1.5769	1.0385	0.5384	0.6923	0.67

Table 2 Parameters of the anisotropic Drucker yield function and anisotropic Drucker potential function of AA 2090-T3 ($n = 2, c = 2$)

		$c_1^{(1)}$	$c_2^{(1)}$	$c_3^{(1)}$	$c_6^{(1)}$	$c_1^{(2)}$	$c_2^{(2)}$	$c_3^{(2)}$	$c_6^{(2)}$
Yield function		3.1638	-4.5130	3.8821	3.4384	0.5926	1.6020	0.3498	1.1341
Plastic potential	case A	2.6452	-6.4631	2.4831	-3.3413	-0.3876	-0.6747	0.5612	0.5870
	case B	-4.4859	1.9722	3.1135	2.8282	1.1742	1.8926	-0.2472	1.4131
	case C	-1.0985	4.2583	-0.8129	2.3019	3.5430	-1.1833	-1.4279	1.8006

Table 3 Anisotropic parameters of Yld2004-18p function of AA 2090-T3 ($a = 8$)

α_1	α_2	α_3	α_4	α_5	α_6	α_7	α_8	α_9
-0.0698	0.9364	0.0791	1.0030	0.5247	1.3631	1.0237	1.0690	0.9543
α_{10}	α_{11}	α_{12}	α_{13}	α_{14}	α_{15}	α_{16}	α_{17}	α_{18}
0.9811	0.4767	0.5753	0.8668	1.1450	-0.0792	1.0516	1.1471	1.4046

$$\mathbf{L}^{(m)} = \begin{bmatrix} (c_2^{(m)} + c_3^{(m)})/3 & -c_3^{(m)}/3 & -c_2^{(m)}/3 & 0 & 0 & 0 \\ -c_3^{(m)}/3 & (c_3^{(m)} + c_1^{(m)})/3 & -c_1^{(m)}/3 & 0 & 0 & 0 \\ -c_2^{(m)}/3 & -c_1^{(m)}/3 & (c_1^{(m)} + c_2^{(m)})/3 & 0 & 0 & 0 \\ 0 & 0 & 0 & c_4^{(m)} & 0 & 0 \\ 0 & 0 & 0 & 0 & c_5^{(m)} & 0 \\ 0 & 0 & 0 & 0 & 0 & c_6^{(m)} \end{bmatrix} \tag{5}$$

Since the coefficient c is recommended to be a constant in Eq. (1), there are six parameters in $\mathbf{L}^{(m)}$ for each component of this yield function. Among the six parameters, four parameters ($c_1^{(m)}, c_2^{(m)}, c_3^{(m)}, c_6^{(m)}$) are used to describe the in-plane anisotropic behavior. The other two parameters can be assumed to be identical with $c_6^{(m)}$ since the out-of-plane properties are difficult to be determined experimentally for sheet metals. Usually, the flexibility of the yield function can be enhanced by increasing the component number n or employing non-AFR. In non-AFR, plastic flow is not necessary to be the normal of yield surface, the yield and potential surface can be defined with different coefficients of the same function, or different functions.

The anisotropic Drucker function is then applied to illustrate the anisotropic plastic behavior of AA2090-T3. The anisotropic mechanical properties of this material are referred in Yoon et al. [52] as listed in Table 1. Considering that c is set to a constant of two for the FCC alloy of AA2090-T3, there are totally 16 anisotropic parameters to be calibrated by experimental data points. Eight of the 16 parameters of the yield function are determined by eight experimental yield stresses, $\sigma_0, \sigma_{15}, \sigma_{30}, \sigma_{45}, \sigma_{60}, \sigma_{75}, \sigma_{90}$ and σ_b . The rest eight parameters of the potential are calibrated by experimental R-values, $r_0, r_{15}, r_{30}, r_{45}, r_{60}, r_{75}, r_{90}$ and r_b . The anisotropic coefficients are obtained

with optimization method and listed in Table 2. The coefficients of the Yld2004-18p (from [52] model are tabulated in Table 3 for the comparison purpose. The loci of yield and plastic potential surface for AA2090-T3 are shown in Figs. 1 and 2 respectively, while Fig. 3 compares the directional normalized initial yield stresses and R-values. These figures show that the anisotropic Drucker function under non-AFR can capture the directional yield stresses and R-values of AA2090-T3 with high accuracy.

Numerical implementation under non-AFR

Under non-AFR, the onset of yielding and the direction of plastic flow are controlled by different functions, as described in Eqs. (6) and (7) respectively.

$$f = \tilde{\sigma}_y(\boldsymbol{\sigma}) - \rho(\bar{\epsilon}^p) = 0 \tag{6}$$

$$d\epsilon^p = \gamma \frac{\partial \tilde{\sigma}_p(\boldsymbol{\sigma})}{\partial \boldsymbol{\sigma}} \tag{7}$$

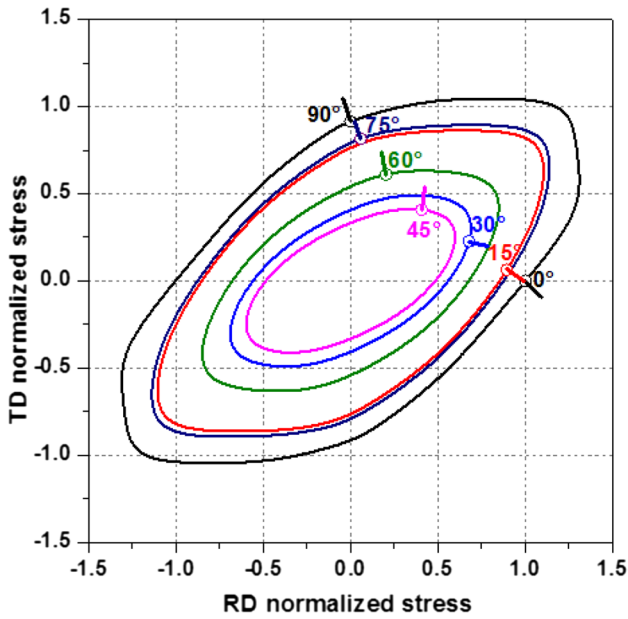


Fig. 1 The yield locus at $\tau_{xy} = \text{const}$ (which equal to the shear stresses of uniaxial tension along $0^\circ, 15^\circ, 30^\circ, 45^\circ, 60^\circ, 75^\circ$ and 90°) for AA2090-T3. The lines at the hollow circles show the normal of yield surface

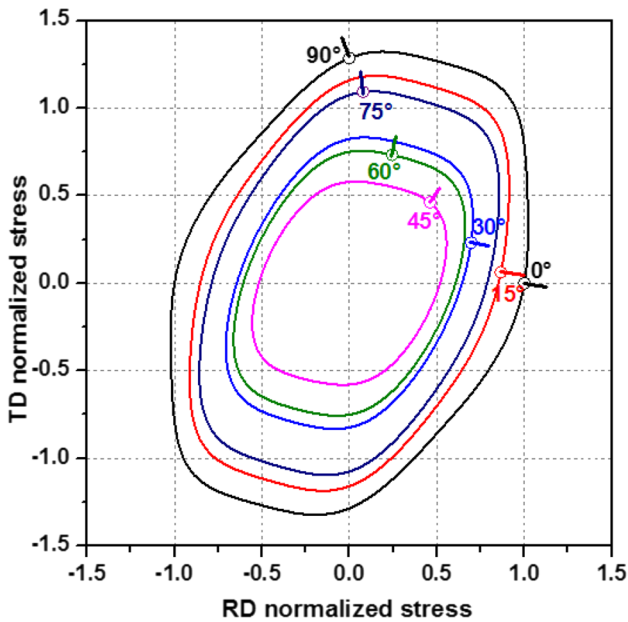
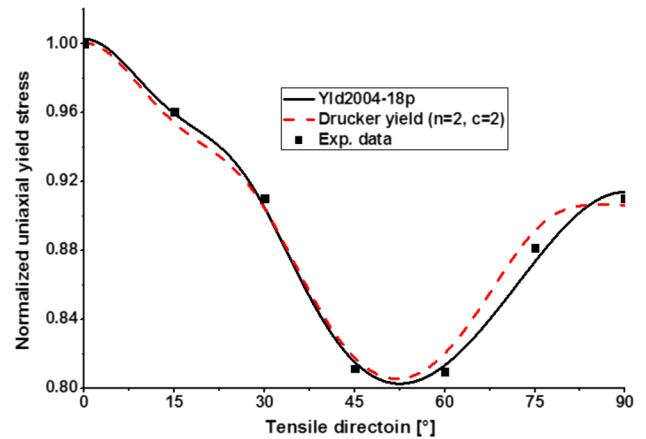
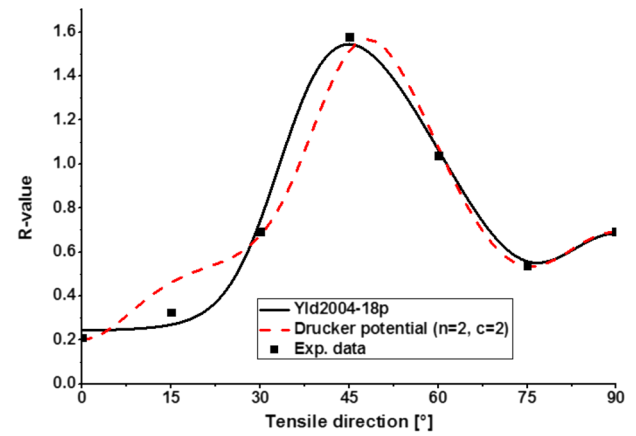


Fig. 2 The loci of plastic potential (case A) at $\tau_{xy} = \text{const}$ (which equal to the shear stresses of uniaxial tension along $0^\circ, 15^\circ, 30^\circ, 45^\circ, 60^\circ, 75^\circ$ and 90°) for AA2090-T3. The lines at the hollow circles show the direction of plastic flow

where $\tilde{\sigma}_y(\sigma)$ is the yield function, $\tilde{\sigma}_p(\sigma)$ is the plastic potential, $\rho(\bar{\epsilon}^p)$ is a function that describes the hardening behavior relative to the equivalent plastic strain $\bar{\epsilon}^p$, γ is the plastic



(a)



(b)

Fig. 3 Comparison of AA 2090-T3 predicted by anisotropic Drucker function under non-AFR (case A) and Yld2004-18 function under AFR: (a) normalized tensile yield stresses; (b) R-values

multiplier and $d\bar{\epsilon}^p$ is the plastic strain increment vector. The relationship between the equivalent plastic strain increment $d\bar{\epsilon}^p$ and γ under non-AFR is determined according to the principal of equivalent plastic work,

$$d\bar{\epsilon}^p = \frac{\sigma d\epsilon^p}{\tilde{\sigma}_y(\sigma)} = \gamma \frac{\sigma \frac{\partial \tilde{\sigma}_p(\sigma)}{\partial \sigma}}{\tilde{\sigma}_y(\sigma)} = \gamma \frac{\tilde{\sigma}_p(\sigma)}{\tilde{\sigma}_y(\sigma)} \quad (8)$$

where $\tilde{\sigma}_p(\sigma)$ is a first order homogenous function.

For a given strain increment $\Delta\epsilon_{n+1}$ at the current time step, the trial stress can be calculated by assuming that all the deformation is elastically recovered:

$$\sigma_{n+1}^T = \sigma_n + C\Delta\epsilon_{n+1} \quad (9)$$

where σ_{n+1}^T is the trial stress state, σ_n is the stress state at previous time step and C is the tensor of elastic moduli. Plastic deformation takes place if

$$f_{n+1} = \tilde{\sigma}_y(\boldsymbol{\sigma}_{n+1}^T) - \rho(\bar{\boldsymbol{\epsilon}}_n^p) > 0 \tag{10}$$

The predictor–corrector scheme can be solved with Newton–Raphson method to update the state variables to satisfy the consistency condition. For the k -th iteration, the increment of plastic multiplier can be obtained by linearization of the consistency condition:

$$d(\gamma_{n+1})^{(k+1)} = -\frac{(f_{n+1})^{(k)}}{\left(\frac{\partial f_{n+1}}{\partial \gamma_{n+1}}\right)^{(k)}} \tag{11}$$

where

$$\left(\frac{\partial f_{n+1}}{\partial \gamma_{n+1}}\right)^{(k)} = \left(\frac{\partial \tilde{\sigma}_y(\boldsymbol{\sigma}_{n+1})}{\partial \gamma_{n+1}}\right)^{(k)} - \left(\frac{\partial \rho(\bar{\boldsymbol{\epsilon}}_{n+1}^p)}{\partial \gamma_{n+1}}\right)^{(k)} \tag{12}$$

$$\rho(\bar{\boldsymbol{\epsilon}}_{n+1}^p) = \rho(\bar{\boldsymbol{\epsilon}}_n^p) + H_{n+1}d\bar{\boldsymbol{\epsilon}}_{n+1}^p = \rho(\bar{\boldsymbol{\epsilon}}_n^p) + \gamma_{n+1}H_{n+1}\frac{\tilde{\sigma}_p(\boldsymbol{\sigma}_{n+1})}{\tilde{\sigma}_y(\boldsymbol{\sigma}_{n+1})} \tag{13}$$

According to the chain rule,

$$\frac{\partial \tilde{\sigma}_y(\boldsymbol{\sigma}_{n+1})}{\partial \gamma_{n+1}} = \frac{\partial \tilde{\sigma}_y(\boldsymbol{\sigma}_{n+1})}{\partial \boldsymbol{\sigma}_{n+1}} \frac{\partial \boldsymbol{\sigma}_{n+1}}{\partial \gamma_{n+1}} \tag{14}$$

$$\frac{\partial \rho(\bar{\boldsymbol{\epsilon}}_{n+1}^p)}{\partial \gamma_{n+1}} = H_{n+1}\frac{\tilde{\sigma}_p(\boldsymbol{\sigma}_{n+1})}{\tilde{\sigma}_y(\boldsymbol{\sigma}_{n+1})} + \gamma_{n+1}H_{n+1}\left(\frac{1}{\tilde{\sigma}_y(\boldsymbol{\sigma}_{n+1})}\frac{\partial \tilde{\sigma}_p(\boldsymbol{\sigma}_{n+1})}{\partial \boldsymbol{\sigma}_{n+1}}\frac{\partial \boldsymbol{\sigma}_{n+1}}{\partial \gamma_{n+1}} - \frac{\tilde{\sigma}_p(\boldsymbol{\sigma}_{n+1})}{\tilde{\sigma}_y^2(\boldsymbol{\sigma}_{n+1})}\frac{\partial \tilde{\sigma}_y(\boldsymbol{\sigma}_{n+1})}{\partial \boldsymbol{\sigma}_{n+1}}\frac{\partial \boldsymbol{\sigma}_{n+1}}{\partial \gamma_{n+1}}\right) \tag{15}$$

with

$$\frac{\partial \boldsymbol{\sigma}_{n+1}}{\partial \gamma} = -\mathbf{C}\frac{\partial \tilde{\sigma}_p(\boldsymbol{\sigma}_{n+1})}{\partial \boldsymbol{\sigma}_{n+1}} \tag{16}$$

By combining Eqs. (11–16), the increment of plastic multiplier is obtained

$$d(\gamma_{n+1})^{(k+1)} = \frac{(f_{n+1})^{(k)}}{\left(g_{yp} + H_{n+1}\frac{\tilde{\sigma}_p(\boldsymbol{\sigma}_{n+1})}{\tilde{\sigma}_y(\boldsymbol{\sigma}_{n+1})} + \gamma_{n+1}H_{n+1}\left(\frac{\tilde{\sigma}_p(\boldsymbol{\sigma}_{n+1})}{\tilde{\sigma}_y(\boldsymbol{\sigma}_{n+1})}g_{yp} - g_{pp}\right)\right)^{(k)}} \tag{17}$$

where

$$g_{yp} = \frac{\partial \tilde{\sigma}_y(\boldsymbol{\sigma}_{n+1})}{\partial \boldsymbol{\sigma}_{n+1}}\mathbf{C}\frac{\partial \tilde{\sigma}_p(\boldsymbol{\sigma}_{n+1})}{\partial \boldsymbol{\sigma}_{n+1}}, g_{pp} = \frac{\partial \tilde{\sigma}_p(\boldsymbol{\sigma}_{n+1})}{\partial \boldsymbol{\sigma}_{n+1}}\mathbf{C}\frac{\partial \tilde{\sigma}_p(\boldsymbol{\sigma}_{n+1})}{\partial \boldsymbol{\sigma}_{n+1}} \tag{18}$$

Then the plastic multiplier and equivalent plastic strain can be updated as follows:

$$(\gamma_{n+1})^{(k+1)} = (\gamma_{n+1})^{(k)} + d(\gamma_{n+1})^{(k+1)} \tag{19}$$

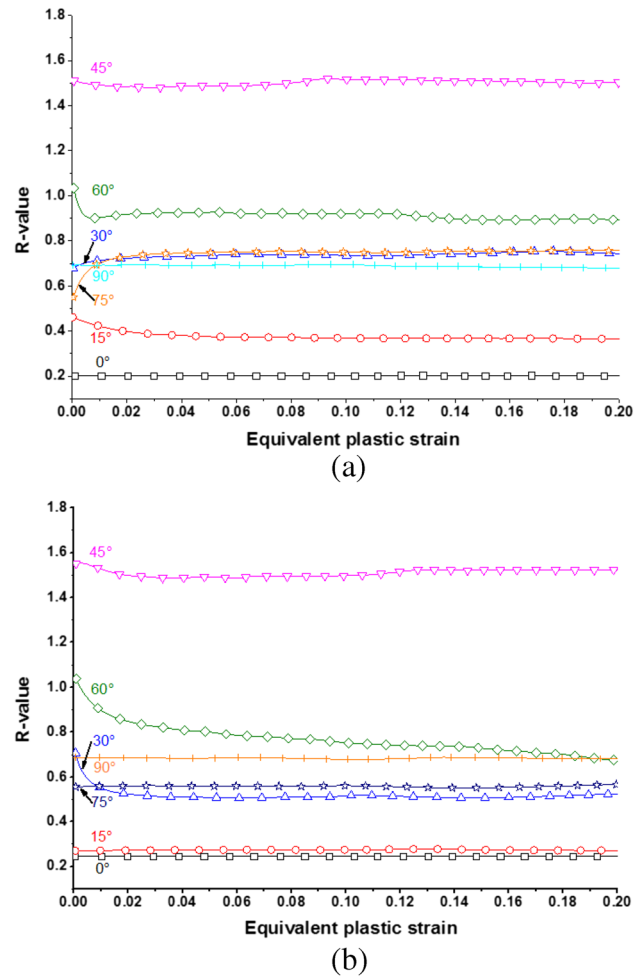


Fig. 4 R-value evolutions during the uniaxial tension predicted by different numerical models. (a) anisotropic Drucker function under non-AFR (case A); (b) Yld2004-18 function under AFR

$$(\bar{\boldsymbol{\epsilon}}_{n+1}^p)^{(k+1)} = (\bar{\boldsymbol{\epsilon}}_{n+1}^p)^{(k)} + d(\gamma_{n+1})^{(k+1)}\left(\frac{\tilde{\sigma}_p(\boldsymbol{\sigma}_{n+1})}{\tilde{\sigma}_y(\boldsymbol{\sigma}_{n+1})}\right)^{(k)} \tag{20}$$

The increment of plastic multiplier can be solved with the semi-implicit algorithm, which ensures the consistency condition. The integration algorithm and the anisotropic functions are implemented into ABAQUS/Explicit via the user-defined material subroutine. Numerical simulations are performed for uniaxial tension of a single cubic element in every 15° from RD. It should be mentioned that the R-value does not keep constant during the uniaxial tension in numerical simulations with both yield functions. It is observed to vary with the equivalent plastic strain as shown in Fig. 4. Figure 5 depicts the variation of R-values at the initial yielding and at a certain equivalent plastic strain of 20% in different orientations. The R-values

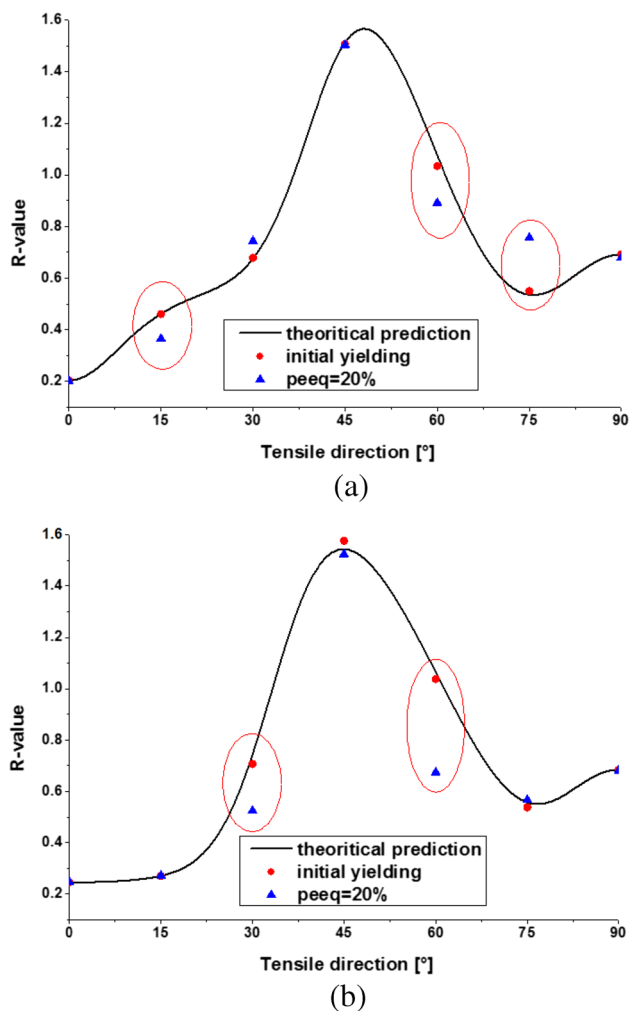


Fig. 5 The variation of R-value at initial yielding and at a constant value of equivalent plastic strain. The solid curve is the results of theoretical evaluation. (a) anisotropic Drucker function under non-AFR (case A); (b) yld2004-18p under AFR

are consistent with the theoretical prediction at the initial yielding, and obvious deviations can be observed at large plastic deformation in some orientations as marked in Fig. 5. The magnitudes of the deviations depend on the plastic flow directions and tensile directions. The accuracy of the predicted R-values at the initial yielding is determined by the potential function. It should be noted that the R-values are evaluated in the uniaxial tension of a single cubic element, the deviation occurs both under AFR and non-AFR. The reason of the R-values changing with the increase of plastic deformation may be due to the shape of the yield surface, the angle between the loading direction and the normal direction of the yield surface, and the predictor–corrector algorithm, which makes it difficult to accurately determine the relative movement of yield points even in proportional loading and isotropic hardening condition. During the calculation and returning process of

elastic-prediction and plastic-correction, the guess stress and guess strain of each incremental step are related to the loading direction, and the guess strain needs to determine the values of the elastic strain increment and the plastic strain increment by the plastic algorithm, and the calculation of the plastic strain increment is related to the normal direction of the yield point and the used returning algorithm. It should be noted that, for many yield functions, such as Yld2004 and Drucker functions, the loading direction and the normal direction at the yield point are likely to be inconsistent in unidirectional tension, so the stress state obtained after convergence by elastic predictor-plastic correction iteration is not exactly proportional to the previous stress state, but falls around the expected point depending on the used returning algorithm and the curvature of the yield surface near the point. That means the yield surface actually located after convergence is not the same as the yield surface obtained by the proportional expansion of the original yield surface, which will make the normal at the yield point of the two consecutive incremental steps change, which may results in a small change of the R-value. This change accumulates with further loading and the increment of plastic strain, resulting in significant changes in the R-values in some directions. So the angle between the loading direction and the flow direction may not keep constant, but vary as the plastic deformation increases. This variation of R-values may cause the difficulty in accurately predicting the anisotropic behavior in metal forming, such as earing prediction. It should be noted that, the exact mechanism of the change of R-values during different unidirectional tension is not clear, and the causes and influencing factors need to be further analyzed.

Cup drawing simulations of AA2090-T3

The numerical simulation of cup drawing test for AA2090-T3 is carried out to evaluate the performance of the anisotropic Drucker function. The dimensions of the tools are given in details by Yoon et al. [52]. In this study, 3D solid elements are employed in the numerical simulation of cup deep drawing. Taking the advantage of axis symmetry of the model, a quarter part of the cup is analyzed with enforced symmetric boundary conditions. The swift hardening law $\bar{\sigma} = 646 \times (0.025 + \bar{\epsilon})^{0.227} \text{ MPa}$. The coefficient of friction is set to be 0.1 for all the contact surfaces under Coulomb model. The blank holding force is 5.5kN for the quarter model.

The final geometry and corresponding Drucker equivalent stress distribution of the drawn cups are shown in Fig. 6. The comparison of cup height profile between 0° and 90° predicted by the anisotropic Drucker and Yld2004-18p function is shown in Fig. 7. Both models agree well with the earing profile measured from experiments. Particularly, the small

Fig. 6 The deformed configuration of completely drawn cups using the anisotropic Drucker function under non-AFR for AA2090-T3

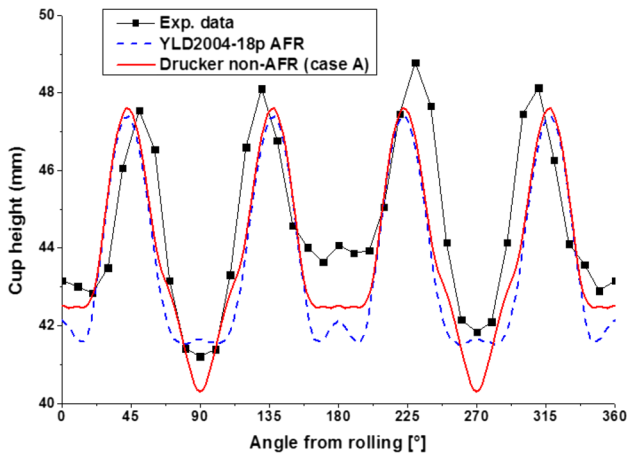
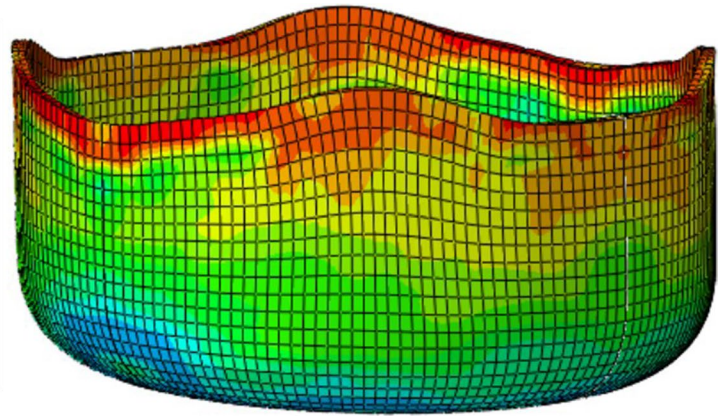
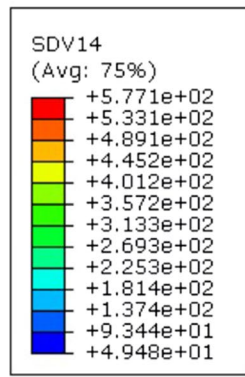


Fig. 7 The cup height profiles predicted by the anisotropic Drucker function under non-AFR and Yld2004-18p under AFR

ear around 0° and the height difference between 0° and 90° are well predicted by the anisotropic Drucker function.

The computation time of the numerical simulations for these two models is also compared in Table 4, which shows that about 40% of the computation efficiency can be improved with the anisotropic Drucker function. Lou and Yoon [30] reported that, compared with the Yld2004-18p function, 60% of computation cost can be reduced with the Drucker function for some simple tension case without contact, which is 20% higher than the percent of computation cost reduction in this study. This is because

there is no need for the computation of contact in the numerical simulation of simple tensile test in Lou and Yoon [30], while it takes a lot of time to solve the contact problem in the simulation of cup deep drawing in this study.

Discussions

It is generally accepted that prediction for six or eight ears in cup deep drawing for strong anisotropic metals requires advanced yield and potential functions that can accurately describe the directional yield stresses and R-values. In spite of the yield stress and R-value directionalities, the shapes of yield and potential surface also influence the prediction of earing profile for cup deep drawing.

As mentioned above, one of the effective methods to enhance the flexibility of yield function is to use non-AFR where the yield and potential function can be different. Usually, the anisotropic coefficients can be determined by the optimization method according to the experimental yield stresses and R-values respectively. As the number of parameters increases, the calibration becomes more and more difficult. The optimized anisotropic parameters are different for different initial guess points. Taking the isotropically calculated values as the initial guess, a local optimization result may be reached. So a series of initial values produced with experimental design methods is used to evaluate the influence of parameter calibration. In this study, three sets of parameters representing different

Table 4 Comparison of computational cost between the Yld2004-18p and anisotropic Drucker function

Software	Abaqus 6.14-4 Explicit/Double Precision/1 cpu		
System	64-bit		
Processor	Intel(R) Core(TM) i5-2430 M CPU@2.40 GHz		
Algorithm	Semi-implicit		
Computation time	Yld2004-18p	Anisotropic Drucker	Reduction of computational cost
	04:37:16	02:47:29	40%

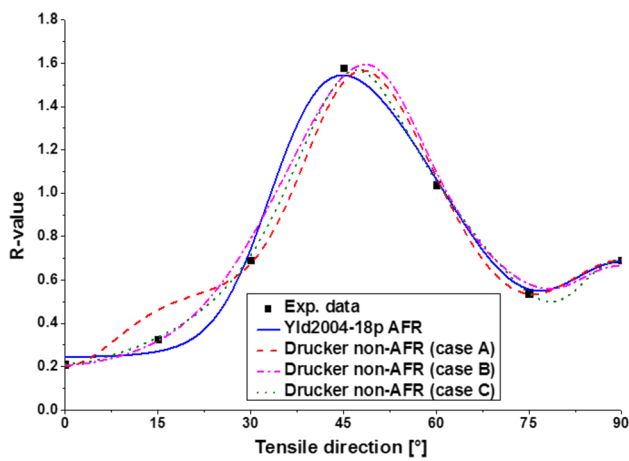


Fig. 8 The directional R-values predicted by the anisotropic Drucker function with different anisotropic coefficients

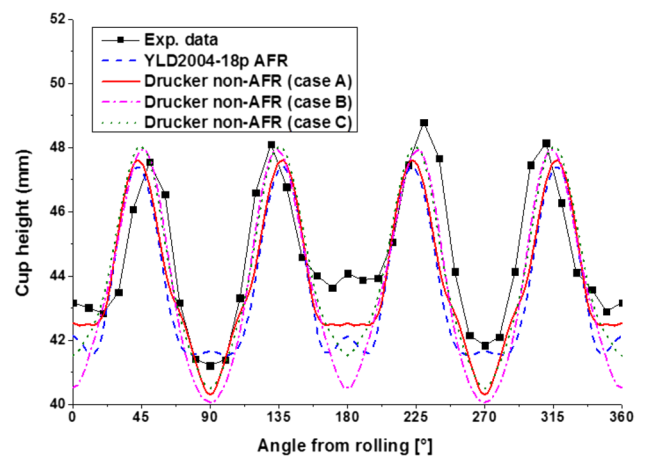


Fig. 10 Comparison of the cup height profiles predicted by different potential functions

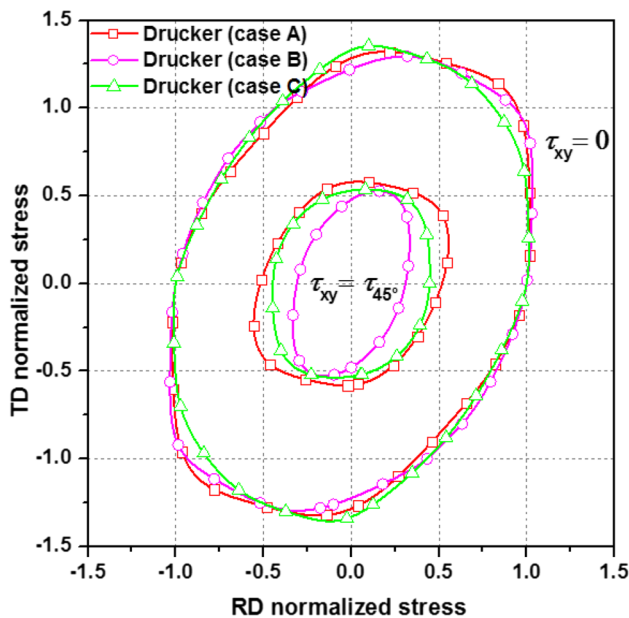


Fig. 9 Comparison of plastic potential shapes predicted by the Drucker function with different anisotropic coefficients

shapes of the anisotropic Drucker plastic potential are analyzed for AA2090-T3, denoted as case A, B and C with anisotropic parameters summarized in Table 2. Figures 8 and 9 show the directional R-values and the corresponding plastic potential shapes predicted from the anisotropic Drucker plastic potential function for the three sets of parameters respectively. Three sets of plastic potential functions coupling with the same Drucker yield function are used to predict the earing of cup drawing for AA2090-T3. The predicted cup height profiles for different plastic potential are shown in Fig. 10. It should be noticed that the small ear around 0° can only be predicted for case A. Both case B and case C fail to predict the small ear, although the theoretical

Table 5 Four models by combining the anisotropic Drucker function and Yld2004-18p function under non-AFR (parameters are listed in Tables 2 and 3)

	Yield function	Plastic potential function
Yld2004-Yld2004	Yld2004-18p	Yld2004-18p
Drucker-Yld2004	Anisotropic Drucker	Yld2004-18p
Yld2004-Drucker	Yld2004-18p	Anisotropic Drucker (case A)
Drucker-Drucker	Anisotropic Drucker	Anisotropic Drucker (case A)

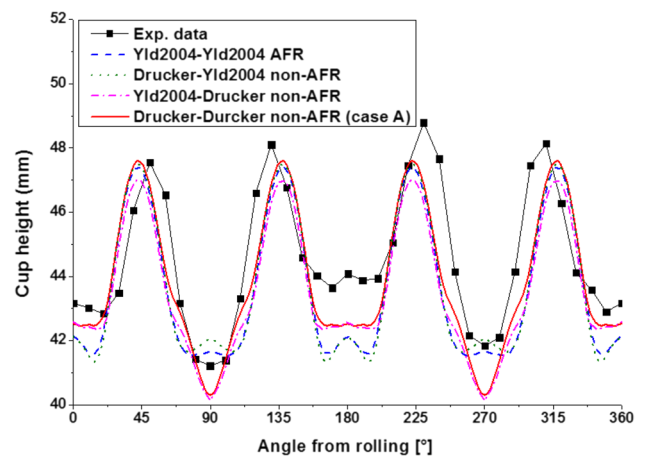


Fig. 11 Comparison of the cup height profiles predicted by the Drucker and Yld2004-18p functions under non-AFR

R-values obtained in both cases are more consistent with the experimental results than that in case A. So the improvement of accuracy of prediction for r-values do not mean the synchronously improvement in prediction the earing profile for strong anisotropic phenomena of deep drawing for AA2090-T3. This

needs further investigation but cannot be explained currently due to the complex stress state in cup deep drawing.

To further investigate the influences of different shapes of yield surface and plastic potential surface on earing prediction, four cases combined from the anisotropic Drucker function and Yld2004-18p function under non-AFR are performed as listed in Table 5. The comparison of the cup height profiles predicted by these models are shown in Fig. 11, which shows that all the four models can predict the small ear around 0°. The earing profiles can be divided into two groups according to different plastic potentials: one group corresponds to the anisotropic Drucker plastic potential, and the other is corresponding to the Yld2004-18p plastic potential. The cup height predicted by the anisotropic Drucker plastic potential is higher at the interval between 0° and 15° and lower around 90° than that predicted with the Yld2004-18p plastic potential. Using Yld2004-18p as the plastic potential function, the different yield functions only changes the local cup height, such as at 15° and 90°, without changing the overall cup height. For the anisotropic Drucker plastic potential function, the overall cup height is obviously lowered when Yld2004-18p function is used as the yield criterion. The comparison of earing profiles predicted by different combination of the Drucker and Yld2004-18 functions under non-AFR proves that, in spite of the uniaxial tensile yield stresses and R-values, both the yield surface and plastic potential locus affect the predicted earing profile. In comparison with the yielding function, the potential function has stronger influence in accurately predicting the earing profile, and the prediction accuracy can be significant improved by reasonable selection for potential functions.

Conclusions

The recently proposed anisotropic Drucker function based on stress invariants under non-AFR is implemented into the finite element software ABAQUS/Explicit with semi-implicit algorithm. The numerical application of anisotropic Drucker function is verified with uniaxial tensile simulation of a single element. The comparison of the cup drawing simulation shows that the earing profile of AA2090-T3 predicted by the Drucker function is consistent with experimental measurement. About 40% computation time can be reduced with the Drucker function under non-AFR compared with the Yld2004-18p function under AFR.

Comparison of the earing profile predicted by different anisotropic Drucker potential functions reveals that a proper shape of plastic potential is very important to predict the small ear around 0° for AA2090-T3. Numerical simulation with various combination of the yield and potential functions reveals that the height and earing profile in the cup drawing simulation can be strongly influenced by the shapes of yield and potential surfaces.

Appendix: Derivatives of the anisotropic Drucker function

The derivatives of the anisotropic Drucker function in Eq. (1) can be calculated as below:

$$\frac{\partial f(\sigma_{ij})}{\partial \sigma_{ij}} = \frac{1}{n} \sum_{m=1}^n \left\{ \frac{\partial f(\sigma_{ij})^{(m)}}{\partial \sigma_{ij}} \right\} \tag{21}$$

where

$$f(\sigma_{ij})^{(m)} = \left[\left(J_2^{(m)} \right)^3 - c \left(J_3^{(m)} \right)^2 \right]^{1/6} \tag{22}$$

According to the chain rule,

$$\begin{aligned} \frac{\partial f(\sigma_{ij})^{(m)}}{\partial \sigma_{ij}} &= \frac{\partial f(\sigma_{ij})^{(m)}}{\partial J_2^{(m)}} \frac{\partial J_2^{(m)}}{\partial s_{ij}^{(m)}} \frac{\partial s_{ij}^{(m)}}{\partial \sigma_{ij}} + \frac{\partial f(\sigma_{ij})^{(m)}}{\partial J_3^{(m)}} \frac{\partial J_3^{(m)}}{\partial s_{ij}^{(m)}} \frac{\partial s_{ij}^{(m)}}{\partial \sigma_{ij}} \\ &= \left(\frac{\partial f(\sigma_{ij})^{(m)}}{\partial J_2^{(m)}} \frac{\partial J_2^{(m)}}{\partial s_{ij}^{(m)}} + \frac{\partial f(\sigma_{ij})^{(m)}}{\partial J_3^{(m)}} \frac{\partial J_3^{(m)}}{\partial s_{ij}^{(m)}} \right) \frac{\partial s_{ij}^{(m)}}{\partial \sigma_{ij}} \end{aligned} \tag{23}$$

with

$$\frac{\partial f(\sigma_{ij})^{(m)}}{\partial J_2^{(m)}} = \frac{1}{2} \left(\left(J_2^{(m)} \right)^3 - c \left(J_3^{(m)} \right)^2 \right)^{-5/6} \left(J_2^{(m)} \right)^2 \tag{24}$$

$$\frac{\partial f(\sigma_{ij})^{(m)}}{\partial J_3^{(m)}} = -\frac{c}{3} \left(\left(J_2^{(m)} \right)^3 - c \left(J_3^{(m)} \right)^2 \right)^{-5/6} J_3^{(m)} \tag{25}$$

$$\frac{\partial J_2^{(m)}}{\partial s_{ij}^{(m)}} = \begin{bmatrix} -\left(s_{22}^{(m)} + s_{33}^{(m)} \right) \\ -\left(s_{11}^{(m)} + s_{33}^{(m)} \right) \\ -\left(s_{22}^{(m)} + s_{11}^{(m)} \right) \\ 2s_{23}^{(m)} \\ 2s_{13}^{(m)} \\ 2s_{12}^{(m)} \end{bmatrix}^T \tag{26}$$

$$\frac{\partial J_3^{(m)}}{\partial s_{ij}^{(m)}} = \begin{bmatrix} s_{22}^{(m)} s_{33}^{(m)} - \left(s_{23}^{(m)} \right)^2 \\ s_{11}^{(m)} s_{33}^{(m)} - \left(s_{13}^{(m)} \right)^2 \\ s_{11}^{(m)} s_{22}^{(m)} - \left(s_{12}^{(m)} \right)^2 \\ 2s_{12}^{(m)} s_{13}^{(m)} - 2s_{11}^{(m)} s_{23}^{(m)} \\ 2s_{12}^{(m)} s_{23}^{(m)} - 2s_{22}^{(m)} s_{13}^{(m)} \\ 2s_{23}^{(m)} s_{13}^{(m)} - 2s_{33}^{(m)} s_{12}^{(m)} \end{bmatrix}^T \tag{27}$$

$$\frac{\partial s_{ij}^{(m)}}{\partial \sigma_{ij}} = \begin{bmatrix} (c_2^{(m)} + c_3^{(m)})/3 & -c_3^{(m)}/3 & -c_2^{(m)}/3 & 0 & 0 & 0 \\ -c_3^{(m)}/3 & (c_3^{(m)} + c_1^{(m)})/3 & -c_1^{(m)}/3 & 0 & 0 & 0 \\ -c_2^{(m)}/3 & -c_1^{(m)}/3 & (c_1^{(m)} + c_2^{(m)})/3 & 0 & 0 & 0 \\ 0 & 0 & 0 & c_4^{(m)} & 0 & 0 \\ 0 & 0 & 0 & 0 & c_5^{(m)} & 0 \\ 0 & 0 & 0 & 0 & 0 & c_6^{(m)} \end{bmatrix} \quad (28)$$

Acknowledgements The authors would like to thank the Guangdong National Natural Science Foundation under the grant number 2021A1515010598 and the National Natural Science Foundation of China (Grant No.52075423; U2141214) and the Fundamental Research Funds for the Central Universities (Grant No. xtr012019004 & zrz2017027).

Declarations

Declaration of interest statement The authors declare that they have no known competing financial interests or personal relationships that could have appeared to influence the work reported in this paper.

References

- Aretz H, Barlat F (2013) New convex yield functions for orthotropic metal plasticity. *Int J Non-Linear Mech* 51:97–111
- Banabic D, Aretz H, Comsa DS, Paraianu L (2005) An improved analytical description of orthotropy in metallic sheets. *Int J Plast* 21:493–512
- Banabic D, Barlat F, Cazacu O, Kuwabara T (2020) Advances in anisotropy of plastic behaviour and formability of sheet metals. *Int J Mater Form* 13:749–787
- Barlat F, Lian K (1989) Plastic behavior and stretchability of sheet metals. Part I: a yield function for orthotropic sheets under plane stress conditions. *Int J Plast* 5:51–66
- Barlat F, Lege DJ, Brem JC (1991) A six-component yield function for anisotropic materials. *Int J Plast* 7:693–712
- Barlat F, Maeda Y, Chung K, Yanagawa M, Brem JC, Hayashida Y, Lege DJ, Matsui K, Murtha SJ, Hattori S, Becker RC, Makosey S (1997) Yield function development for aluminum alloy sheets. *J Mech Phys Solids* 45:1727–1763
- Barlat F, Brem JC, Yoon JW, Chung K, Dick RE, Lege DJ, Pourboghrat F, Choi S-H, Chu E (2003) Plane stress yield function for aluminum alloy sheets – Part I: theory. *Int J Plast* 19:1297–1319
- Barlat F, Aretz H, Yoon JW, Karabin ME, Brem JC, Dick RE (2005) Linear transformation-based anisotropic yield functions. *Int J Plast* 21:1009–1039
- Cazacu O (2019) New mathematical results and explicit expressions in terms of the stress components of Barlat et al. (1991) orthotropic yield criterion. *Int J Solids Struct* 176–177:86–95
- Cazacu O (2020) New expressions and calibration strategies for Karafillis and Boyce (1993) yield criterion. *Int J Solids Struct* 185–186:410–422
- Cazacu O, Barlat F (2001) Generalization of Drucker's yield criterion to orthotropy. *Math Mech Solids* 6:613–630
- Cazacu O, Barlat F (2004) A criterion for description of anisotropy and yield differential effects in pressure-insensitive metals. *Int J Plast* 20:2027–2045
- Cazacu O, Plunkett B, Barlat F (2006) Orthotropic yield criterion for hexagonal closed packed metals. *Int J Plast* 22:1171–1194
- Chen Z, Wang Y, Lou YS (2022) User-friendly anisotropic hardening function with non-associated flow rule under the proportional loadings for BCC and FCC metals. *Mech Mater* 165:104190
- Comsa DS, Banabic D (2008) Plane-stress yield criterion for highly-anisotropic sheet metals. *Numisheet 2008*, Interlaken, Switzerland, 43–48
- Cvitanic V, Vlcek F, Lozina Z (2008) A finite element formulation based on nonassociated plasticity for sheet metal forming. *Int J Plast* 24:646–687
- Dick RE, Yoon JW (2018) Plastic anisotropy and failure in thin metal: Material characterization and fracture prediction with an advanced constitutive model and polar EPS (effective plastic strain) fracture diagram for AA3014-H19. *Int J Solids Struct* 151:195–213
- Hill R (1948) A theory of the yielding and plastic flow of anisotropic metals. *Proc R Soc Lond Ser A* 193:281–297
- Hill R (1979) Theoretical plasticity of textured aggregates. *Math Proc Cambridge Philos Soc* 85:179–191
- Hill R (1990) Constitutive modeling of orthotropic plasticity in sheet metal. *J Mech Phys Solids* 38:405–417
- Hosford WF (1979) On yield loci of anisotropic cubic metals. *Proc North Am Metalwork Res Conf* pp 191–197
- Hou Y, Min JY, Stoughton TB, Lin JP, Carsley JE, Carlson BE (2020) A non-quadratic pressure-sensitive constitutive model under non-associated flow rule with anisotropic hardening: modeling and validation. *Int J Plast* 135:102808
- Hou Y, Min JY, Guo N, Shen YF, Lin JP (2021) Evolving asymmetric yield surfaces of quenching and partitioning steels: characterization and modeling. *J Mater Process Technol* 290:116979
- Hou Y, Lee M-G, Lin JP, Min JY (2022) Experimental characterization and modeling of complex anisotropic hardening in quenching and partitioning (Q&P) steel subject to biaxial non-proportional loadings. *Int J Plast* 156:103347
- Hu Q, Yoon JW (2021) Analytical description of an asymmetric yield function (Yoon2014) by considering anisotropic hardening under non-associated flow rule. *Int J Plast* 140:102978
- Hu Q, Yoon JW, Manopulo N, Hora P (2021a) A coupled yield criterion for anisotropic hardening with analytical description under associated flow rule: modeling and validation. *Int J Plast* 136:102882
- Hu Q, Yoon JW, Stoughton TB (2021b) Analytical determination of anisotropic parameters for Poly6 yield function. *Int J Mech Sci* 201:106467
- Karafillis AP, Boyce MC (1993) A general anisotropic yield criterion using bounds based a transformation weighting tensor. *J Mech Phys Solids* 41:1859–1886
- Lee EH, Choi H, Stoughton TB, Yoon JW (2019) Combined anisotropic and distortion hardening to describe directional response with Bauschinger effect. *Int J Plasticity* 122:73–88
- Lou YS, Yoon JW (2018) Anisotropic yield function based on stress invariants for BCC and FCC metals and its extension to ductile fracture criterion. *Int J Plast* 101:125–155
- Lou YS, Huh H, Yoon JW (2013) Consideration of strength differential effect in sheet metals with symmetric yield functions. *Int J Mech Sci* 66:214–223
- Lou YS, Zhang SJ, Yoon JW (2019) A reduced Yld 2004 function for modeling of anisotropic plastic deformation of metals under triaxial loading. *Int J Mechan Sci* 161:105027
- Lou YS, Zhang SJ, Yoon JW (2020) Strength modeling of sheet metals from shear to plane strain tension. *Int J Plast* 134:102813
- Lou YS, Zhang C, Zhang SJ, Yoon JW (2022) A general yield function with differential and anisotropic hardening for strength modelling under various stress states with non-associated flow rule. *Int J Plast* 158:103414
- Mohr D, Dunand M, Kim KH (2010) Evaluation of associated and non-associated quadratic plasticity models for advanced

- high strength steel sheets under multi-axial loading. *Int J Plast* 26:939–956
36. Park T, Chung K (2012) Non-associated flow rule with symmetric stiffness modulus for isotropic-kinematic hardening and its application for earing in circular cup drawing. *Int J Solids Struct* 49:3582–3593
 37. Park N, Stoughton TB, Yoon JW (2019) A criterion for general description of anisotropic hardening considering strength differential effect with non-associated flow rule. *Int J Plast* 121:76–100
 38. Safaei M, Zang SL, Lee MG, Waele WD (2013) Evaluation of anisotropic constitutive models: mixed anisotropic hardening and non-associated flow rule approach. *Int J Mech Sci* 73:53–68
 39. Safaei M, Lee MG, Zang SL, Waele WD (2014) An evolutionary anisotropic model for sheet metals based on non-associated flow rule approach. *Comput Mater Sci* 81:15–29
 40. Smith J, Liu WK, Cao J (2015) A general anisotropic yield function for pressure-dependent materials. *Int J Plast* 75:2–21
 41. Soare S, Barlat F (2010) Convex polynomial yield functions. *J Mech Phys Solids* 58:1804–1818
 42. Soare SC, Barlat F (2011) A study of the Yld 2004 yield function and one extension in polynomial form: a new implementation algorithm, modeling range, and earing predictions for aluminum alloy sheets. *Eur J Mech A/Solids* 30:807–819
 43. Soare S, Yoon JW, Cazacu O (2008) On the use of homogeneous polynomials to develop anisotropic yield functions with applications to sheet forming. *Int J Plast* 24:915–944
 44. Stoughton TB (2002) A non-associated flow rule for sheet metal forming. *Int J Plast* 18:687–714
 45. Stoughton TB, Yoon JW (2004) A pressure-sensitive yield criterion under a non-associated flow rule for sheet metal forming. *Int J Plast* 20(4-5):705–731
 46. Stoughton TB, Yoon JW (2009) Anisotropic hardening and non-associated flow in proportional loading of sheet metals. *Int J Plast* 25:1777–1817
 47. Taherizadeh A, Green DE, Ghaei A, Yoon JW (2010) A non-associated constitutive model with mixed iso-kinematic hardening for finite element simulation of sheet metal forming. *Int J Plast* 26:288–309
 48. Vrh M, Halilović M, Starman B, Comsa D-S, Banabic D (2014) Capability of the BBC2008 yield criterion in predicting the earing profile in cup deep drawing simulations. *Eur J Mech A/Solids* 45:59–74
 49. Yoon JW, Barlat F, Chung K, Pourboghraat F, Yang DY (1998) Influence of initial back stress on the earing prediction of drawn cups for planar anisotropic aluminum sheets. *J Mater Process Technol* 80–81:433–437
 50. Yoon JW, Barlat F, Chung K, Pourboghraat F, Yang DY (2000) Earing predictions based on asymmetric nonquadratic yield function. *Int J Plast* 16:1075–1104
 51. Yoon JW, Barlat F, Dick RE, Chung K, Kang TJ (2004) Plane stress yield function for aluminum alloy sheets - Part II: FE formulation and its implementation. *Int J Plast* 20:705–731
 52. Yoon JW, Barlat F, Dick RE, Karabin ME (2006) Prediction of six or eight ears in a drawn cup based on a new anisotropic yield function. *Int J Plast* 22:174–193
 53. Yoon JW, Dick RE, Stoughton TB (2007) Earing prediction in cup drawing based on non-Associated flow rule. *AIP Conf Proc* 908:685–690
 54. Yoon JW, Lou YS, Yoon JH, Glazoff MV (2014) Asymmetric yield function based on the stress invariants for pressure sensitive metals. *Int J Plast* 56:184–202
 55. Yoshida F, Hamasaki H, Uemori T (2013) A user-friendly 3D yield function to describe anisotropy of steel sheet. *Int J Plast* 45:119–139

Publisher's note Springer Nature remains neutral with regard to jurisdictional claims in published maps and institutional affiliations.

Springer Nature or its licensor (e.g. a society or other partner) holds exclusive rights to this article under a publishing agreement with the author(s) or other rightsholder(s); author self-archiving of the accepted manuscript version of this article is solely governed by the terms of such publishing agreement and applicable law.